

Contactless Inline *IV* Measurement of Solar Cells Using an Empirical Model

Philipp Kunze,* Johannes M. Greulich, Ammar Tummali, Wiebke Wirtz, Hannes Hoeffler, Nico Woehrle, Stefan Glunz, Stefan Rein, and Matthias Demant

The current–voltage measurement is the most important measurement in solar cell quality control. As the contacting process of cells results in mechanical stress and consumes a significant amount of measurement time, this work presents an *IV* characterization based on contactless measurements only. An empirical model is introduced that can derive the full *IV* curve and *IV* parameters as the open-circuit voltage, short-circuit current density, fill factor, and efficiency. As a basis, a series of photoluminescence and contactless electroluminescence images and spectral reflectance measurements are used. An advantage of the model's convolutional neural network design lies in the semantic compression of local image structures across the input data. Within an ablation study, it is shown that the empirical model is well suited to combine these data sources, which is the optimal input configuration for contactless *IV* derivation. The accuracy, e.g., with an error in efficiency of 0.035%_{abs} and correlation of over 99%, is similar to comparing two contacting *IV* measurement devices. The contactless *IV* curves also have a close fit to their contacted counterparts. Within simulations on module level, it is demonstrated that contactless binning performs as well as contacting binning and does not result in any additional mismatch loss.

or series resistance (R_s) can be determined to describe the properties of the cells as well as to monitor or optimize processes.

Contacting the cells for *IV* measurement is the standard up to now, but it involves some drawbacks. One disadvantage relates to a limited throughput of the contacted *IV* measurement. On the one hand, up to 900 ms are lost due to contacting and decontacting, which is a multiple compared to the actual measurement time.^[1] On the other hand, the measurement time itself should not be too short to reduce hysteresis effects.^[2,3] Another disadvantage is related to material costs. The cell is subjected to mechanical stress, which can lead to damage or breakage, so that maximum breakage rates of, e.g., 0.1% are usually specified for *IV* measurement devices. In addition, the contacting unit is also exposed to wear, so that it has to be replaced after a few cycles, which means material costs on the one hand and downtime on the other.


Recently, Greulich et al. presented the first approach regarding fully contactless *IV* measurements, achieving high measurement accuracy compared to contacted measurements.^[4] By this method, low errors of 0.5%_{abs} and 2.1 mV from the contacted measurement were achieved on average for the determination of efficiency and open-circuit voltage, respectively. This approach is based on a combination of suns-photoluminescence (suns-PL), contactless electroluminescence (EL), spectral reflectance, and the luminescence spectrum derived by different contactless measurement techniques. A contactless measurement of a solar cell's pseudo-*IV* characteristics via suns-PL has been introduced by Trupke et al. involving PL measurements at several illumination intensities.^[5] Additionally, contactless EL measurements can be performed for determination of parallel and series resistance.^[6,7] By partial shading of the measurement sample, it is possible to determine the series resistance, as has been shown quantitatively.^[8] The spectral reflectance can be measured inline, e.g., via white illumination and a spectrometer.^[9] The luminescence spectrum can be analyzed to calculate the external quantum efficiency.^[10–13]

We adopt the approach by Greulich et al. and propose an empirical model for *IV* determination purely based on contactless measurement techniques targeted on using less and only inline applicable measurement techniques for industrial usage.

1. Introduction

The current–voltage (*IV*) values of solar cells represent the heart of their characterization in industry and research. In the current state-of-the-art, the cell is automatically contacted with some contact bars on the front and back side, whereupon the *IV* characteristic can be measured. Based on this, (model) parameters like open-circuit voltage (V_{oc}), short-circuit current density (J_{sc}),

P. Kunze, J. M. Greulich, A. Tummali, W. Wirtz,^[†] H. Hoeffler, N. Woehrle, S. Glunz, S. Rein, M. Demant
Division Photovoltaics
Fraunhofer Institute for Solar Energy Systems (ISE)
Heidenhofstrasse 2, 79110 Freiburg, Germany
E-mail: philipp.kunze@ise.fraunhofer.de

 The ORCID identification number(s) for the author(s) of this article can be found under <https://doi.org/10.1002/solr.202200599>.

^[†]Present address: Institute for Solar Energy Research Hamelin, Am Ohrberg 1, 31860 Emmerthal, Germany

© 2022 The Authors. Solar RRL published by Wiley-VCH GmbH. This is an open access article under the terms of the Creative Commons Attribution License, which permits use, distribution and reproduction in any medium, provided the original work is properly cited.

DOI: 10.1002/solr.202200599

For this, we utilize a series of PL images with varying illumination intensities and integration times in order to determine the cell characteristics on multiple points of the pseudo-*IV* curve. Additionally, we apply contactless EL imaging using partial shading to approximate series resistances' influence. As an indication regarding short-circuit current density, we also include the spectral reflectance into the model which can be measured contactlessly inline.

As empirical model, we develop a convolutional neural network (CNN) to derive the solar cell *IV* characteristics and investigate its prediction quality on a big dataset of industrial heterojunction (HJT) solar cells of different quality classes. The convolutional architecture enables the model to also include local defect structure patterns into the analysis instead of mean values only because we do not expect defect areas to necessarily scale linearly with their impact on the solar cell. Moreover, the CNN model enables the assessment of superimposing defect structures across multiple measurements. We build the model in such a way that it is able to fuse information coming from different data sources (EL, PL, and $R(\lambda)$). Here, we vary the number and combination of measurements in order to derive an optimal measurement configuration for inline applicability. We evaluate the model with regard to multiple parameters: 1) typical *IV* parameters as V_{oc} , J_{sc} , η , fill factor (FF), 2) full *IV* curve, and 3) contactless binning accuracy.

CNNs have shown promising results in processing spatially resolved measurement data in recent publications. Rodrigues Abreu et al. have shown an approach in which they predict ten points on the module's *IV* curve based on EL images using ten CNNs.^[14] In comparison, we develop a single model that processes various input data from contactless measurements of solar cells to derive an *IV* curve with a sampling rate at 100 curve positions. In other works, it was demonstrated that *IV* parameters can be learned from EL, PL, or thermography images of solar cells and wafers.^[15–24] Beyond that, imaging measurement methods were mostly used for defect detection.^[25–45]

We expect our model for contactless *IV* determination to compensate the drawbacks of the contacted method mentioned above. As there is no time for contacting needed, there is the potential of saving a large part of the measurement time which may allow lower cycle times and higher throughput and thus decrease equipment costs. As no mechanical stress is applied to the cells, breakage rates are reduced. Moreover, we demonstrate correlations of up to 99%, precise *IV* curve derivation, and a contactless binning accuracy of over 92% leading to no additional mismatch losses in the final module. Also, costs coming from contact units' wear and switching times will not be present. However, other measurement parts would be added, such as shutters to partially shade the sample, which are not necessary for the contacted measurement.

In summary, our contributions are 1) an empirical contactless model for the determination of *IV* parameters and the *IV* curve, 2) the extension of the model so that additional spectral reflectance measurements can be integrated, 3) an extensive evaluation based on an ablation study of the input data, and 4) an investigation of the impact of contactless binning at the module level.

2. Approach

2.1. Contactless Measurements

As basis for contactless inline *IV* measurement, we use contactless EL measurements as well as up to six suns-PL measurements. In **Figure 1**, the contactless EL images can be seen in (a–b). They involve partial shading of the cell leading to a current flow of generated charge carriers so that series resistance effects, such as finger interruptions, become visible in the luminescence pictures, e.g., finger interruptions appear as lighter regions within the image. In Figure 1c–h, the suns-PL measurements are shown. They include different measurement settings which are chosen so that they cover reasonable sampling points on the cells pseudo, meaning R_s -shifted, *IV* curve, starting at V_{oc} in (c),

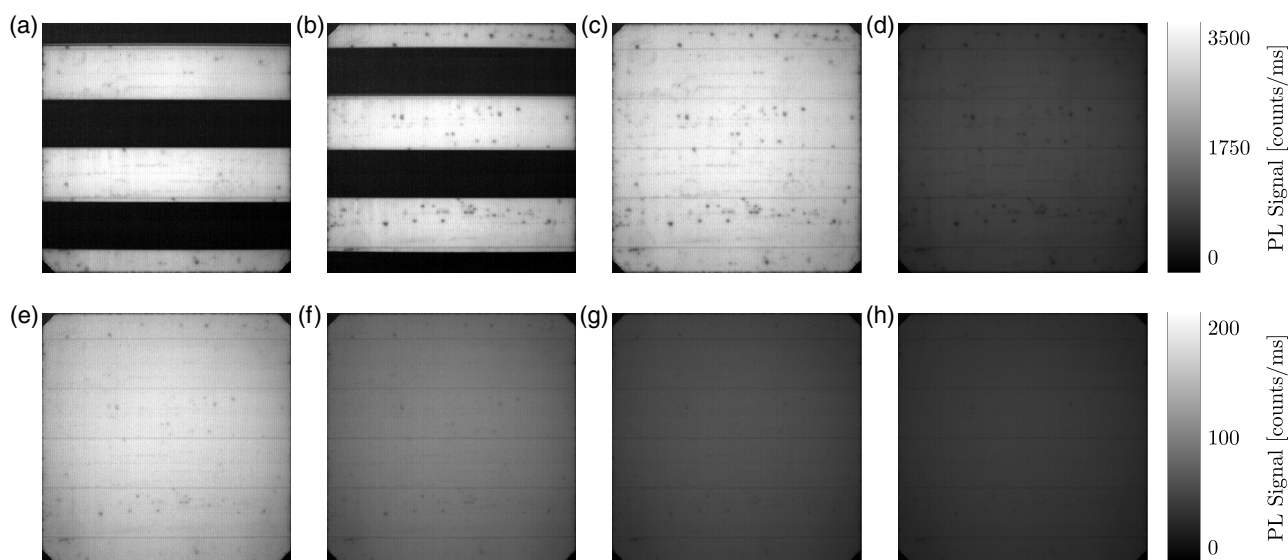


Figure 1. Example contactless EL in (a,b) and suns-PL measurements (c–h) of one cell. The color bar in the first row indicates the PL signal for (a–d); the color bar in the second row indicates the PL signal for (e–h).

stepping along the pseudo- IV curve in (d–e) until reaching the region of the maximum power point (MPP) in (f–h).

Besides spatially resolved measurements, we also include measurements of the spectral reflection ($R(\lambda)$) into our model, which were determined along the center trace of each sample only. The data include three reflection curves positioned next to each other on the cells' surface in the wavelength range from 360 to 1100 nm and a resolution of 2 nm in wavelength.

2.2. Empirical Model for Contactless IV Derivation

As empirical model, we develop a number of CNNs getting the measurement data mentioned as input and predicting the IV characteristics as output. CNNs consist of a series of convolutional, pooling, and nonlinear unit layers. Step by step, they reduce the spatial dimension of the input while increasing the semantic expressiveness with regard to the target parameters. We utilize variations of the DenseNet architecture.^[46] However, we expect similar modern CNN architectures to be adaptable for this task as well.

The empirical models developed are regression models predicting the scalar IV parameters but also target the problem of data fusion of EL and PL images, as well as $R(\lambda)$ measurement curves. In addition, we adapted the architecture to derive the full IV curve instead of only scalar parameters. The architectural approach chosen can be seen in **Figure 2**. The first row shows the processing of image-like data. They are concatenated and passed to the CNN_{PL} producing 128 feature maps of size 7×7 . When only using image data, those are passed to a final network part CNN_{IV} used to derive the respective IV parameters as output.

When it comes to fusing the $R(\lambda)$ curves into the model, it can be extended as shown in the second row in **Figure 2**. The data viewed as a table holding the three $R(\lambda)$ measurements M_i with their reflectance values r_{ij} as columns at all wavelengths considered λ_j , where i refers to the measurement index and j to the respective wavelength. n is the number of measurement entries per $R(\lambda)$ measurement. The matrix is passed to a small model we call CNN_{SR} . The convolutional kernels cover all columns, i.e., they have a size of 3×3 , in order to value the homogeneity of

all measurement lines. However, the pooling layers are applied column-wise, i.e., they have a size of 1×5 . The resulting $R(\lambda)$ features f have the same three-column shape with m rows. The mean of each row is calculated and upsampled to m $R(\lambda)$ feature maps of size 7×7 , so that the $R(\lambda)$ information is available at each pixel's position. As the image and the $R(\lambda)$ data are of same spatial size now, they can be concatenated and passed to CNN_{IV} as additional information.

The models are either targeted to predict single scalar values or a vector representing the main IV parameters or the IV curve, respectively. As scalar output, we consider the open-circuit voltage V_{oc} , the short-current density J_{sc} , the FF, and the power at MPP P_{mpp} or efficiency η . Regarding IV curve derivation, we used 100 points on the IV curve at fixed voltage positions as target vector. The points are densely sampled around $V \approx 0$ V, $V \approx V_{MPP}$, and $V \approx V_{oc}$ to be more accurate in those most relevant regions.

In addition, a custom loss function was used for the IV curve range from 0 V to about V_{mpp} . It has been noticed in preliminary tests that there is a slight fluctuation in the predictions in this range. By adding an approximation of the first and second derivatives into the loss function, false fluctuations of neighboring points are suppressed. The loss function is described by Equation (1).

$$L = L_1(\hat{\mathbf{i}}, \mathbf{i}) + L_1(\hat{\mathbf{i}}_{1-40}, \dot{\mathbf{i}}_{1-40}) + L_1(\hat{\mathbf{i}}_{1-40}, \ddot{\mathbf{i}}_{1-40}) \quad (1)$$

Here, L_1 stands for the L1 loss function, $\hat{\mathbf{i}}$ is the current vector predicted by the network, \mathbf{i} is the current vector measured contacted, and \mathbf{i}_{1-40} and $\dot{\mathbf{i}}_{1-40}$ are the first 40 entries of \mathbf{i} and $\dot{\mathbf{i}}$, respectively. The dots are referring to the difference of neighboring points as approximation of the derivations.

2.3. Contactless Binning and Influence on Module Level

We also perform a contactless binning of the cells and investigate the influence on module level regarding mismatch losses, i.e., the power loss due to nonidentical cells built into the module. For this, we define binning classes and sort the cells

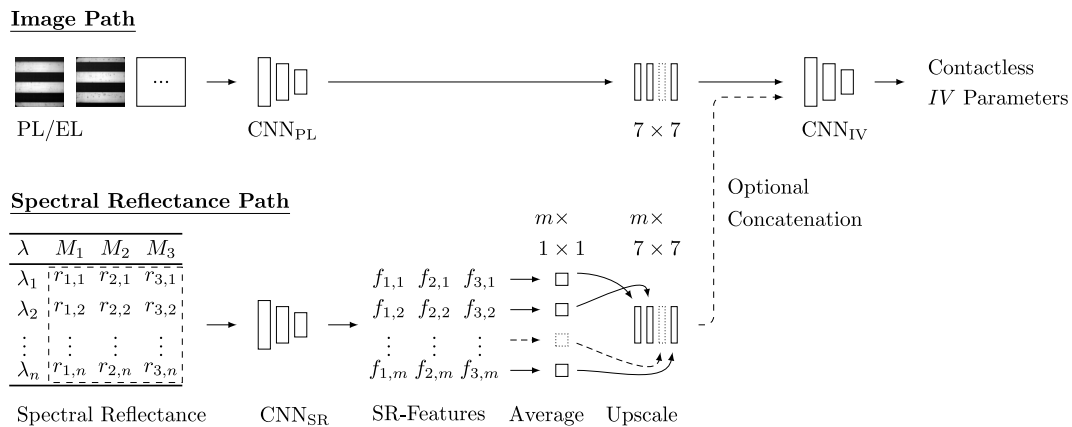


Figure 2. Schematic architecture of the empirical model for contactless IV determination. To fuse different type of data, the first line shows the processing of image-like data, while the second one shows the processing of curve data as spectral reflectance measurements.

according to their power at MPP P_{mpp} . We do this with regard to both contacted and contactless measurements to compare. Besides the evaluation of the binning accuracy, we simulate the modules to compute their mismatch losses for each bin class which we would expect from binning in a common 60 cells module with cells contacted in series with bypass diodes. We calculate the mismatch loss P_{ml} as defined in Equation (2).

$$P_{\text{ml}} = P_{\text{sum}} - P_{\text{sim}} \quad (2)$$

Here, P_{sim} holds the simulated module power and P_{sum} is the sum of all powers of the respective 60 cells at MPP (see Equation (3))

$$P_{\text{sum}} = \sum_{i=1}^{60} P_{\text{mpp},i} \quad (3)$$

with $P_{\text{mpp},i}$ being the power of the i th cell at MPP.

3. Experiments

As dataset, we use 4500 industrially manufactured HJT solar cells of size $158 \times 158 \text{ mm}^2$. The cells come from four different quality classes. In addition, we include about 150 cells sorted out during production to increase the heterogeneity of the dataset. All cells were measured with PL, partially shaded PL, and contacted IV. For some of them, additional spectral reflectance measurements have been carried out. The measurement settings for the PL and partially shaded PL measurements are shown in **Table 1**. For all PL images, homogeneous illumination was used. PL1 is at V_{oc} and PL4 roughly at MPP as described in the approach. PL2 is on the pseudo-IV curve between V_{oc} and MPP. PL3–6 are located at or around the MPP. For the contactless EL measurement, two partially shaded measurements were conducted using the measurement settings shown in the last row of Table 1. Both PL and contactless EL were performed with a measurement system from ISRA Vision and finally scaled to a size of $224 \times 224 \text{ px}^2$. For 800 of the cells, additional spectral reflectance measurements were done with a Zeiss OFR104. As a reference, contacted IV measurements were carried out with a measuring system from halm GmbH.

Table 1. PL measurement times.

| Homogeneous PL Measurements | | |
|----------------------------------|--------------|-------------------|
| Measurement | Illumination | Illumination Time |
| PL1 | 1 sun | 0.9 ms |
| PL2 | 0.3 suns | 3 ms |
| PL3 | 0.065 suns | 15 ms |
| PL4 | 0.046 suns | 28 ms |
| PL5 | 0.029 suns | 40 ms |
| PL6 | 0.024 suns | 58 ms |
| Partially Shaded PL Measurements | | |
| Each half | 1.36 suns | 0.9 ms |

As model, we use a variation of the DenseNet^[46] implemented in PyTorch.^[47] For optimization, we use the Adam optimizer^[48] and vary within a grid search the learning rate and decay. The models were optimized on a Nvidia GeForce RTX 2080 Ti with a batch size of 30 samples. Furthermore, the full dataset was randomly subdivided into three datasets: the training dataset with 70% of the samples and the validation and test dataset with 15% of the data each. The models were trained on the training dataset. The best model was selected with the validation dataset and all results calculated on the test dataset to make sure the models generalize well.

3.1. Experiment 1: Contactless IV Parameter

We trained empirical models to derive the main IV parameters from contactlessly measured data. We focus on V_{oc} , J_{sc} , FF, and P_{mpp} . By a variation of the inputs, we want to find a good input configuration. All variations tested are shown, e.g., in **Table 2**. The second and third column show whether and which EL and PL measurements were used in each of the 12 different configurations. Variation 1 uses only the partially shaded EL images. Gradually, more measurement images are added starting with the PL4 (at MPP) and PL1 (at V_{oc}) until in variation 9 all measurement images are used. In variations 10–12, no partially shaded PL images are included. In addition, each of these variations is performed once with and once without $R(\lambda)$, as indicated in the second row. The models are evaluated based on the mean absolute error (MAE) and the Pearson correlation coefficient ρ .

3.2. Experiment 2: Contactless IV Curve

Within this experiment, we investigate the quality of the empirical contactless models with respect to the prediction of the complete IV curve. We consider three input variations: 1) only partially shaded PL images, 2) partially shaded PL images and all six homogeneous PL images, and 3) all mentioned images plus $R(\lambda)$ measurement as input data. We compare the empirical models with respect to their MAE and correlation coefficient at each point of the IV curve with the contacted IV curve as reference.

Additionally, for the best model based on MAE, we perform a qualitative analysis of exemplary IV curves and the corresponding cells. For this purpose we use a medium quality cell, as well as cells with particularly low V_{oc} and J_{sc} , respectively, and investigate the cell having the highest error to assess the quality and stability of the model in such edge cases.

3.3. Experiment 3: Contactless Binning

In Experiment 3, we investigate the contactless binning in comparison to the contacted binning and examine what influence these two variants would have on the module level. For this purpose, the cells are sorted into four binning classes based on the contacted and contactless power measurements from experiment 1. The classes start at 5300 mW and proceed in 50 mW steps up to 5500 mW. In terms of efficiency, this corresponds approximately to 0.2% large bin classes from 21.5% to 22.3%.

The quality of the contactless binning is evaluated on the one hand using the consistency with the contacted binning as

Table 2. MAEs and correlation coefficients regarding P_{mpp} and FF for all input variations.

| Input Variation | | | P_{mpp}/η | | | | | | FF | | | |
|-----------------|--------|------------------|----------------------|---------------|--------|-------------------|---------------|-------------|----------------------|--------|-------------------|-------------|
| | | | Without $R(\lambda)$ | | | With $R(\lambda)$ | | | Without $R(\lambda)$ | | With $R(\lambda)$ | |
| | | | MAE [mW] | MAE [%abs] | ρ | MAE [mW] | MAE [%abs] | ρ | MAE [%abs] | ρ | MAE [%abs] | ρ |
| No. | Shaded | PL Sequence | | | | | | | | | | |
| 1 | Yes | | 10.23 | 0.041 | 0.97 | 9.70 | 0.039 | 0.99 | 0.110 | 0.90 | 0.113 | 0.93 |
| 2 | Yes | 4 | 10.27 | 0.042 | 0.97 | 10.15 | 0.041 | 0.98 | 0.111 | 0.75 | 0.103 | 0.94 |
| 3 | Yes | 1 | 9.65 | 0.039 | 0.98 | 9.58 | 0.039 | 0.99 | 0.112 | 0.79 | 0.104 | 0.95 |
| 4 | Yes | 1,4 | 8.97 | 0.036 | 0.98 | 9.24 | 0.037 | 0.99 | 0.092 | 0.93 | 0.083 | 0.96 |
| 5 | Yes | 1, 3, 4 | 9.02 | 0.037 | 0.98 | 8.87 | 0.036 | 0.99 | 0.097 | 0.92 | 0.079 | 0.97 |
| 6 | Yes | 1, 4, 5 | 9.08 | 0.037 | 0.98 | 8.81 | 0.035 | 0.99 | 0.096 | 0.92 | 0.089 | 0.96 |
| 7 | Yes | 1, 3, 4, 5 | 9.83 | 0.040 | 0.98 | 9.61 | 0.039 | 0.99 | 0.091 | 0.93 | 0.079 | 0.97 |
| 8 | Yes | 1, 3, 4, 5, 6 | 9.49 | 0.039 | 0.98 | 9.53 | 0.039 | 0.99 | 0.097 | 0.92 | 0.088 | 0.95 |
| 9 | Yes | 1, 2, 3, 4, 5, 6 | 9.89 | 0.04 | 0.98 | 9.42 | 0.038 | 0.99 | 0.099 | 0.93 | 0.076 | 0.97 |
| 10 | No | 1 | 12.40 | 0.050 | 0.96 | 10.78 | 0.044 | 0.98 | 0.147 | 0.81 | 0.147 | 0.87 |
| 11 | No | 4 | 13.57 | 0.055 | 0.95 | 0.83 | 0.149 | 0.87 | 0.137 | 0.84 | 0.149 | 0.87 |
| 12 | No | 1, 2, 3, 4, 5, 6 | 11.94 | 0.049 | 0.96 | 0.85 | 0.129 | 0.92 | 0.130 | 0.86 | 0.129 | 0.92 |

reference and on the other hand by comparing the mean mismatch losses of the contacted and contactless binning by means of module simulations under standard test conditions (STCs) assuming a standard module topology of 60 cells in series subdivided in three strings with bypass diodes, as described in Section 2.3. We use only the cells of the test dataset, so that 10 modules were simulated per variation. We define \bar{P}_{ml} as the mean contactless binning loss of these modules, $\bar{P}_{ml,ref}$ as the mean contacted binning loss as reference, and their difference as $\Delta\bar{P}_{ml} = \bar{P}_{ml} - \bar{P}_{ml,ref}$. If $\Delta\bar{P}_{ml}$ is 0 W, contactless and contacted binning would perform equally well on module level. If the value is positive, contacted binning performs better; if it is negative, contactless is better.

4. Experimental Results

4.1. Experiment 1— Results: Contactless IV Parameters

The contactless method works well for all investigated IV parameters on the test dataset. **Table 2** and **3** show the results for all variations investigated; the second and third column refer to the respective input data variation in terms of images. For each quality parameter, the results for models without and with $R(\lambda)$ measurements are shown in separate columns. Per parameter evaluation, the subsequent columns present the MAE as well as the Pearson correlation coefficient ρ having the contacted measurement as reference. The best input configuration per parameter is highlighted in bold. For J_{sc} , V_{oc} , and FF, networks with all available input data

Table 3. MAEs and correlation coefficients regarding V_{oc} and J_{sc} for all input variations.

| Input Variation | | | V_{oc} | | | | J_{sc} | | | |
|-----------------|--------|------------------|----------------------|--------|-------------------|-------------|-------------------------------|--------|-------------------------------|-------------|
| | | | Without $R(\lambda)$ | | With $R(\lambda)$ | | Without $R(\lambda)$ | | With $R(\lambda)$ | |
| | | | MAE [mV] | ρ | MAE [mV] | ρ | MAE [mA cm ⁻²] | ρ | MAE [mA cm ⁻²] | ρ |
| No. | Shaded | PL Sequence | | | | | | | | |
| 1 | Yes | | 0.73 | 0.99 | 0.42 | 0.99 | 0.067 | 0.81 | 0.062 | 0.84 |
| 2 | Yes | 4 | 0.65 | 0.99 | 0.42 | 0.99 | 0.061 | 0.82 | 0.062 | 0.85 |
| 3 | Yes | 1 | 0.61 | 0.99 | 0.39 | 0.99 | 0.064 | 0.82 | 0.062 | 0.84 |
| 4 | Yes | 1,4 | 0.49 | 0.99 | 0.38 | 0.99 | 0.062 | 0.83 | 0.062 | 0.84 |
| 5 | Yes | 1, 3, 4 | 0.65 | 0.99 | 0.39 | 0.99 | 0.061 | 0.83 | 0.063 | 0.84 |
| 6 | Yes | 1, 4, 5 | 0.97 | 0.98 | 0.40 | 0.99 | 0.062 | 0.83 | 0.063 | 0.85 |
| 7 | Yes | 1, 3, 4, 5 | 0.56 | 0.99 | 0.43 | 0.99 | 0.063 | 0.82 | 0.061 | 0.85 |
| 8 | Yes | 1, 3, 4, 5, 6 | 0.54 | 0.99 | 0.40 | 0.99 | 0.059 | 0.83 | 0.057 | 0.88 |
| 9 | Yes | 1, 2, 3, 4, 5, 6 | 0.61 | 0.99 | 0.38 | 0.99 | 0.062 | 0.83 | 0.056 | 0.88 |
| 10 | No | 1 | 0.92 | 0.98 | 0.40 | 0.99 | 0.064 | 0.83 | 0.064 | 0.85 |
| 11 | No | 4 | 0.99 | 0.97 | 0.89 | 0.97 | 0.069 | 0.80 | 0.063 | 0.83 |
| 12 | No | 1, 2, 3, 4, 5, 6 | 0.52 | 0.99 | 0.42 | 0.99 | 0.077 | 0.76 | 0.060 | 0.85 |

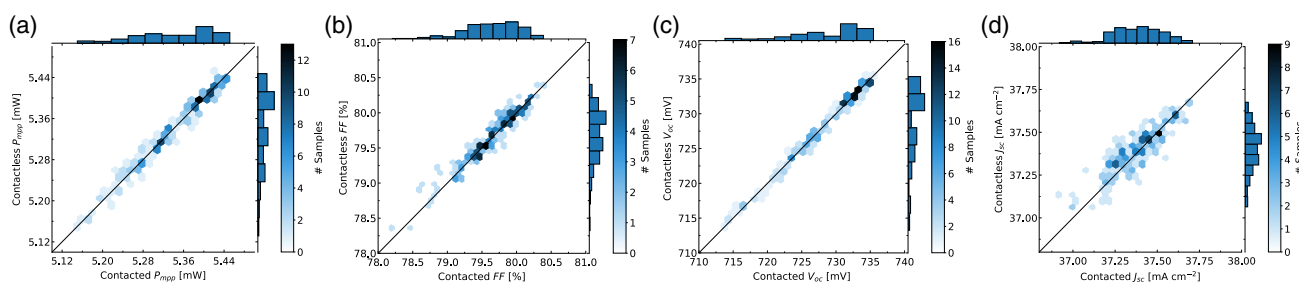


Figure 3. Comparison of the contactless and contacted IV parameters, with the X axis showing the contacted parameter and the Y axis showing the contactless one. P_{mpp} is shown in (a), FF in (b), V_{oc} in (c), and J_{sc} in (d).

have the best results, although these are only slightly better than models with less inputs. Also for η , models with many measurement data achieved the best results, again with very small differences compared to models with fewer inputs.

The results of the best models per parameter are shown in more detail in **Figure 3**. The x-axis shows the contacted measurement and the y-axis the contactless measurement. In case of complete correspondence, all values would lie on the diagonal. It can be seen that especially the contactless P_{mpp} in (a) and the contactless V_{oc} in (c) can be derived accurately. The contactless J_{sc} in (d) shows a slightly higher spread but good correlation as well. The contactless FF in (b) can be derived with similar precision as P_{mpp} and V_{oc} .

Both the inclusion of the partially shaded PL images and the $R(\lambda)$ measurements improve the accuracy of the contactless models. With respect to the partially shaded images, this becomes clear, for example, when comparing variant 9 to variant 12 for P_{mpp} and FF. There, the error increases by about 17% and almost 24%, respectively. Also the $R(\lambda)$ measurement improves the contactless models in most cases. Comparing the MAEs with respect to the V_{oc} of all variations without and with $R(\lambda)$, the errors become on average about 34% lower. However, this behavior is not apparent with the same clarity for the J_{sc} prediction. Here, especially PL5 and PL6, the PL measurements closest to the J_{sc} , seem to be helpful in combination with the $R(\lambda)$.

4.2. Experiment 2—Results: Contactless IV Curve

The contactless IV curves can be derived with low error, and each additional contactless measurement improves the prediction. **Figure 4** shows, on the one hand, the MAE (continuous curves, left y-axis) and, on the other hand, the correlation coefficient (dashed curves, right y-axis) for the considered input variations 1) EL only in green; 2) EL and PL in orange; and 3) EL, PL, and $R(\lambda)$ in blue. It can be seen that the model receiving only the partially shaded EL images performs the worst. Slightly improved results are obtained with the addition of the PL measurements. The prediction accuracy is significantly improved when the reflectance $R(\lambda)$ is also added as input. This is particularly apparent in the area $V < V_{\text{mpp}}$, where the absolute error is reduced by about 34% and the correlation factor increases by 10%_{abs}. In the range of $V > V_{\text{mpp}}$ the absolute error increases, which is due to the fast change of the IV curve; however, still the model receiving all measurements performs best. In all models, the correlation

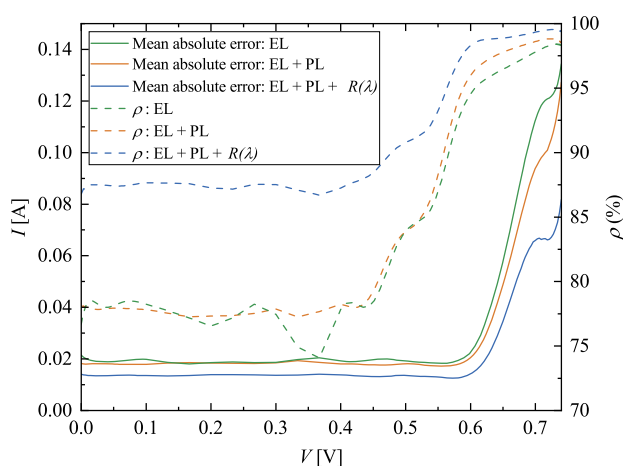


Figure 4. MAE of current of contactless current on IV curve in left y-axis and Pearson correlation factor ρ on the right y-axis for different input scenarios.

coefficients increase over 98% in that region, indicating the correct shape of the curve.

The contactless IV curve of the best model receiving all measurements visually follows well the IV curve measured contacted. **Figure 5** shows the contactless and contacted IV curves as continuous and dashed curves, respectively, for four example cells. Their EL images are shown in Figure 5e–h for visualization purposes only; they have not been used for training. The cell in (e) is a moderate cell with no obvious defects (related to the blue IV curves), while the cell in (f) (related to the red IV curves) is suspected to have slight material inclusions as the black dots indicate and correspondingly a lower V_{oc} . In (g) (related to the green IV curves), on the cell's surface scratches can be seen, which result in a reduced J_{sc} . The EL image in (h) shows the cell with the highest error between contacted and contactless IV curves. In Figure 5b–d, the areas of the IV curve around J_{sc} , MPP, and V_{oc} , respectively, can be viewed in detail. As can be observed, in the area of J_{sc} in (b), the quality of the cell with low J_{sc} is slightly overestimated by about 25 mA, while the curves for the other two cells are in good agreement. Regarding MPP in (c), the curves line up well in all cases. Also for V_{oc} , the curves fit quite well. For the average cell, it matches perfectly. The other two run parallel with an offset of less than 1 mV. In (a–d), the IV curves of the cell with the highest error are shown in red. It can be seen that in the range of J_{sc} it overestimates the current

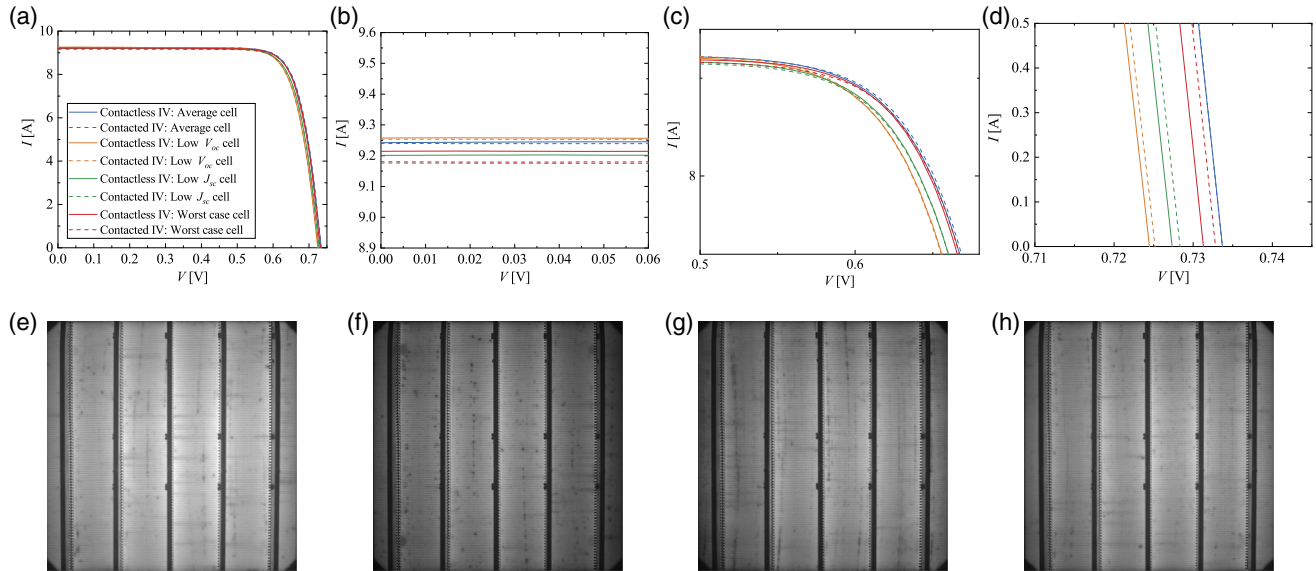


Figure 5. Comparison of contacted (dashed lines) and contactless (solid lines) IV curves for four example cells. In a) the complete IV curves are shown, b–d) show the sections of the IV curves at J_{sc} , MPP, and V_{oc} . The EL images of the example cells with the visible defects are shown in (e–h), with e) showing the average cell (blue), f) showing the low V_{oc} cell (orange), g) showing the low J_{sc} cell (green), and h) showing the cell where the empirical model performed the worst (red).

values by about 30 mA (b), the region around MPP is well mapped (c) and in the range of V_{oc} the curves run parallel with a gap of about 2 mV (d).

4.3. Experiment 3—Results: Contactless Binning

By binning solar cells based on the contactless IV models, high correspondence with the contacted binning can be achieved. In

Table 4. Contactless mismatch losses \bar{P}_{ml} and its difference to contacted mismatch loss $\Delta\bar{P}_{ml}$ for all input variations calculated by module simulations under STC for modules of 60 cells connected in series. The contacted reference is $\bar{P}_{ml,ref,1} = 3.24$ mW for the dataset without $R(\lambda)$ and $\bar{P}_{ml,ref,2} = 3.10$ mW for the dataset with $R(\lambda)$.

| Variation No. | Shaded | PL Sequence | Without $R(\lambda)$ | | | With $R(\lambda)$ | | |
|---------------|--------|------------------|----------------------|--------------------|--------------------------|-------------------|--------------------|--------------------------|
| | | | A | \bar{P}_{ml} [W] | $\Delta\bar{P}_{ml}$ [W] | A | \bar{P}_{ml} [W] | $\Delta\bar{P}_{ml}$ [W] |
| 1 | Yes | | 0.828 | 3.93 | 0.69 | 0.873 | 3.38 | 0.28 |
| 2 | Yes | 4 | 0.833 | 3.43 | 0.19 | 0.862 | 3.16 | 0.06 |
| 3 | Yes | 1 | 0.827 | 3.46 | 0.22 | 0.884 | 3.30 | 0.20 |
| 4 | Yes | 1, 4 | 0.863 | 3.45 | 0.21 | 0.928 | 3.05 | −0.05 |
| 5 | Yes | 1, 3, 4 | 0.848 | 3.51 | 0.28 | 0.8895 | 3.07 | −0.03 |
| 6 | Yes | 1, 4, 5 | 0.843 | 3.3 | 0.06 | 0.917 | 3.13 | 0.03 |
| 7 | Yes | 1, 3, 4, 5 | 0.833 | 3.32 | 0.09 | 0.873 | 3.08 | −0.02 |
| 8 | Yes | 1, 3, 4, 5, 6 | 0.835 | 3.59 | 0.35 | 0.901 | 3.17 | 0.07 |
| 9 | Yes | 1, 2, 3, 4, 5, 6 | 0.823 | 3.32 | 0.08 | 0.901 | 3.10 | 0.00 |
| 10 | No | 1 | 0.790 | 3.6 | 0.36 | 0.862 | 3.11 | 0.01 |
| 11 | No | 4 | 0.784 | 3.64 | 0.4 | 0.851 | 2.98 | 0.12 |
| 12 | No | 1, 2, 3, 4, 5, 6 | 0.797 | 3.6 | 0.37 | 0.862 | 3.26 | 0.16 |

Table 4, the contactless binning accuracy is shown for all input variations with the contacted binning as reference in column 4 and 7. It can be seen that high accuracy can be achieved of up to over 92%. Furthermore, it can be observed that the additional input of $R(\lambda)$ measurement improves the binning quality significantly, on average by almost 6%_{abs}.

Contactless binning is equally well suited for sorting solar cells as contacted binning on module level because the best models achieve the same mismatch loss as the contacted one. In Table 4, the resulting mean mismatch losses of the contactless binning \bar{P}_{ml} for the variations are shown in columns 5 and 8 for a module with 60 cells. Columns 6 and 9 show the mean mismatch loss difference $\Delta\bar{P}_{ml} = \bar{P}_{ml} - \bar{P}_{ml,ref}$ between contactless and contacted binning. The mismatch loss of the contacted binning of the dataset without $R(\lambda)$ is $\bar{P}_{ml,ref,1} = 3.24$ mW and of the dataset with $R(\lambda)$ $\bar{P}_{ml,ref,2} = 3.10$ mW. Without $R(\lambda)$, the power loss is low, ranging from 60 mW to a few 100 mW. With $R(\lambda)$, no mismatch loss is apparent in many cases. In some input variations, e.g., in 4, 5 and 7, the mismatch loss of the contactless binning is even lower than that of the contacted one.

5. Discussion

We have developed models for contactless IV derivation based purely on inline capable measurement technology that can show high correspondence with the current state-of-the-art contacted measurement. In particular, η , V_{oc} , and FF have as low errors as one would expect when comparing two contacting measurement devices. Even the J_{sc} can be measured with a mean error of just 0.056 mA cm^{−2}. Surprisingly, it could also be well approximated based on PL images only, which we attribute to a high correlation between V_{oc} and J_{sc} in our dataset. For this, we used

training datasets of about 830 respectively 3125 HJT cells. The number of samples required for a successful model depends on the heterogeneity and representativeness of the training dataset. In our smallest training dataset with reflectance measurements, already 200 cells per quality class were sufficient to achieve good prediction quality.

There are other parameters which have not yet been integrated into the model. For instance, the shunt resistance R_{sh} , which is of interest for characterization, has not been built into the model so far. Within our approach, the IV region relevant for R_{sh} was not as important because there were no R_{sh} problems in the dataset, so the PL measurement sequence was not optimized for the region around I_{sc} . Regarding empirical models, this point needs to be addressed in the future; however, it has already been shown that this parameter may be derived from contactless measurements.^[6]

The IV curve can be derived with decent accuracy from contactless measurements. It becomes clear, however, that there is a large improvement in the results when all and not only a part of the input data is used. While the addition of PL images to the contactless EL images gives only a slight improvement to the contactless model, with additional $R(\lambda)$ measurements as input there is a significant improvement. This behavior is especially evident for the range $V < V_{mpp}$ and at I_{sc} , which is understandable because the reflection affects the luminescence current and correspondingly the short-circuit current. The current is approximately constant up to MPP and can accordingly be better approximated in this range. However, there exists still potential in exactly this range. In the example cell with low J_{sc} , the IV curve was slightly overestimated in this region. For the evaluated moderate and low V_{oc} cell, the contactless and contacted IV curves match almost precisely.

The binning of the solar cells based on the contactless efficiency η works well. A binning accuracy of significantly more than 90% could be achieved with the contacted measurement as reference. Due to measurement uncertainty, however, inaccuracy is to be expected here as well. Within the module simulations, we are pleased to see that no additional mismatch loss due to contactless binning is to be expected compared to contacted binning, if the $R(\lambda)$ measurement is taken as input.

The contactless IV measurement reduces the measurement time and leads to cost saving. If we assume that the Move-In and Move-Out of the cell takes about 500 ms and add to the measurement times from Table 1 with some buffer, the measurement time for one cell could be about 600–700 ms. This is less than the standard of about 1–1.25 s.^[1] In addition, the cell is not exposed to mechanical damage and there are fewer measurement components that can wear out, which could also save material and maintenance costs.

Nevertheless, contactless IV measurement still has some limitations. One main drawback is that so far no reverse characteristic of the solar cell can be derived without contacting it. Therefore, a suitable contactless measurement technique has to be identified. Also, it is thinkable to perform a classification into reverse-defect and no-reverse-defect, e.g., based on the PL images, as, e.g., indicated by Demant et al. for microcracks in silicon wafers.^[49] In addition, it is likely that the models will need to be retrained if they should be used with a different cell line or

cell type. This point could be particularly relevant, e.g., for research lines because here a lot of very different solar cells are to be expected, to which the models would have to be adjusted.

6. Conclusion

We introduced an empirical approach to contactless IV measurement as an alternative to the contacted measured IV characteristics. For this, we used a number of inline applicable contactless measurements such as partially shaded as well as homogeneously illuminated PL and spectral reflectance measurements. These were combined within a convolutional neural network to calculate IV parameters such as V_{oc} , J_{sc} , FF, and η on the one hand and the full IV curve on the other. We evaluated our approach on a comprehensive set of heterojunction solar cells and performed an ablation study to find the best input measurement configuration.

The contactless models have shown good results in deriving the IV parameters and the full IV curve and we found in module simulation that a contactless binning performs well. Mean deviations of 0.035%_{abs} for η , 0.375 mV for V_{oc} , 0.056 mA cm⁻² for J_{sc} , and 0.076%_{abs} for FF between contactless and contacted measurements were obtained. We found the full contactless IV curves to fit the contacted ones almost precisely. Furthermore, module simulations have shown that contactless binning can replace contacted binning.

We expect that contactless IV measurement can be cheaper than contacting one due to shorter measurement times. This may bring it into interest for future high throughput manufacturing. However, a solution still needs to be found for contactless reverse characteristic measurement and a method for efficient transfer to new cell lines and concepts.

Acknowledgements

This work was partly funded by the German Federal Ministry for Economic Affairs and Climate Action within the project "KISS-PV" (03EE1129A). P.K. would like to thank the Studienstiftung des deutschen Volkes for the support within the scope of his scholarship as well as Momo and Flippa for scientific discussions and moral support. Furthermore, thanks to the PV-TEC Team at Fraunhofer ISE for the support during the experiments.

Open Access funding enabled and organized by Projekt DEAL.

Conflict of Interest

The authors declare no conflict of interest.

Data Availability Statement

The data that support the findings of this study underly third party restrictions. Restrictions apply to the availability of the data, which were used under license for this study. Data are available from the authors with the permission of the third party.

Keywords

characterization, contactless IV, deep learning, empirical model, inline, machine learning, solar cells

Received: June 30, 2022

Revised: July 19, 2022

Published online: August 7, 2022

- [1] M. Alt, S. Fischer, S. Schenk, S. Zimmermann, K. Ramspeck, M. Meixner, in *2018 IEEE 7th World Conf. on Photovoltaic Energy Conversion (WCPEC) (A Joint Conf. 45th IEEE PVSC, 28th PVSEC & 34th EU PVSEC)*, IEEE, Piscataway, NJ **2018**, pp. 3298–3304.
- [2] D. King, J. Gee, B. Hansen, in *Conf. Record of the Twentieth IEEE Photovoltaic Specialists Conf.*, IEEE, Piscataway, NJ **1988**, pp. 555–559.
- [3] R. A. Sinton, H. W. Wilterdink, A. L. Blum, *IEEE J. Photovoltaics* **2017**, 7, 1591.
- [4] J. M. Greulich, W. Wirtz, H. Hoeffler, N. Woehle, M. K. Juhl, O. Kunz, S. Rein, A. W. Bett **2022**.
- [5] T. Trupke, R. Bardos, M. Abbott, J. Cotter, *Appl. Phys. Lett.* **2005**, 87, 093503.
- [6] R. A. Sinton, in *23rd European Photovoltaic Solar Energy Conf.*, Valencia, Spain **2008**, pp. 1157–1159.
- [7] M. Kasemann, L. M. Reindl, B. Michl, W. Warta, A. Schütt, J. Carstensen, *IEEE J. Photovoltaics* **2012**, 2, 181.
- [8] H. Höffler, W. Wirtz, J. M. Greulich, S. Rein, *38th European Photovoltaic Solar Energy Conference and Exhibition*, WIP **2021**, pp. 233–236, <https://doi.org/10.4229/EUPVSEC20212021-2CV.1.5>.
- [9] A. Krieg, J. Greulich, M. Tondorf, S. Rein, in *Proc. 28th European Photovoltaic Solar Energy Conf. and Exhibition*, Paris, France **2013**, pp. 1820–1824.
- [10] K. O. Davis, G. S. Horner, J. B. Gallon, L. A. Vasilyev, K. B. Lu, A. B. Dirriwachter, T. B. Rigdon, E. J. Schneller, K. Ögütman, R. K. Ahrenkiel, in *2017 IEEE 44th Photovoltaic Specialist Conf. (PVSC)*, IEEE, Piscataway, NJ **2017**, pp. 3448–3451.
- [11] A. Paduthol, M. K. Juhl, T. Trupke, *J. Appl. Phys.* **2018**, 123, 023105.
- [12] U. Rau, *Phys. Rev. B* **2007**, 76, 085303.
- [13] T. Kirchartz, A. Helbig, W. Reetz, M. Reuter, J. H. Werner, U. Rau, *Prog. Photovoltaics: Res. Appl.* **2009**, 17, 394.
- [14] S. Rodrigues Abreu, J. Hauch, I. M. Peters, T. Winkler, C. Buerhop-Lutz, C. Brabec, B. Doll, in *36th PV Symp.*, FZJ-2021-02794, Helmholtz-Institut Erlangen-Nürnberg Erneuerbare Energien, Freiburg im Breisgau **2021**, pp. 97–110.
- [15] Y. Buratti, A. Sowmya, R. Evans, T. Trupke, Z. Hameiri, in *2020 47th IEEE Photovoltaic Specialists Conf. (PVSC)*, IEEE, Piscataway, NJ **2020**, pp. 0133–0138.
- [16] A. M. Karimi, J. S. Fada, N. A. Parrilla, B. G. Pierce, M. Koyutürk, R. H. French, J. L. Braid, *IEEE J. Photovoltaics* **2020**, 10, 878.
- [17] A. Kovvali, M. Demant, T. Trötschler, J. Haunschild, S. Rein, in *AIP Conf. Proc.*, AIP Publishing LLC, Lausanne, Switzerland **2018**, vol. 1999, p. 130011.
- [18] M. Demant, P. Virtue, A. Kovvali, X. Y. Stella, S. Rein, *IEEE J. Photovoltaics* **2019**, 9, 1073.
- [19] M. Demant, P. Virtue, A. Kovvali, X. Y. Stella, S. Rein, *IEEE J. Photovoltaics* **2019**, 9, 1064.
- [20] A. S. Kovvali, M. Demant, S. Rein, in *2019 IEEE 46th Photovoltaic Specialists Conf. (PVSC)*, IEEE, Piscataway, NJ **2019**, pp. 3059–3062.
- [21] M. Hoffmann, C. Buerhop-Lutz, L. Reeb, T. Pickel, T. Winkler, B. Doll, T. Würfl, I. Marius Peters, C. Brabec, A. Maier, V. Christlein, *Prog. Photovoltaics: Res. Appl.* **2021**, 29, 920.
- [22] Y. Buratti, A. Sowmya, R. Evans, T. Trupke, Z. Hameiri, *Prog. Photovoltaics: Res. Appl.* **2022**, 30, 276.
- [23] P. Kunze, S. Rein, M. Hemsendorf, K. Ramspeck, M. Demant, *Sol. RRL* **2022**, 6, 2100483.
- [24] M. Demant, L. Kurumundayil, P. Kunze, A. Woernhoer, A. Kovvali, S. Rein, *NeurIPS 2020 Workshop on Tackling Climate Change with Machine Learning* **2020**, <https://www.climatechange.ai/papers/neurips2020/39>.
- [25] B. Su, H. Chen, Z. Zhou, *IEEE Trans. Ind. Electron.* **2021**, 69, 3161.
- [26] R. Pierdicca, E. Malinverni, F. Piccinini, M. Paolanti, A. Felicetti, P. Zingaretti, *Int. Arch. Photogramm. Remote Sens. Spat. Inf. Sci.* **2018**, 42, 2.
- [27] Y. Jiang, C. Zhao, W. Ding, L. Hong, Q. Shen, in *2020 IEEE 9th Data Driven Control and Learning Systems Conf. (DDCLS)*, IEEE, Piscataway, NJ **2020**, pp. 1415–1421.
- [28] J. Balzategui, L. Eciolaza, N. Arana-Arexolaleiba, J. Altube, J.-P. Aguerre, I. Legarda-Ereño, A. Apraiz, in *2019 24th IEEE Inter. Conf. Emerging Technologies and Factory Automation (ETFA)*, IEEE, Piscataway, NJ **2019**, pp. 529–535.
- [29] A. Bartlett, L. Mauch, B. Yang, M. Reuter, L. Stoicescu, in *2018 26th European Signal Processing Conference (EUSIPCO)*, IEEE, Piscataway, NJ **2018**, pp. 2035–2039.
- [30] Z. Ying, M. Li, W. Tong, C. Haiyong, in *2018 Chinese Automation Congress (CAC)*, IEEE, Piscataway, NJ **2019**, pp. 3571–3576.
- [31] O. D. Singh, A. Malik, V. Yadav, S. Gupta, S. Dora, *Multimed. Tools Appl.* **2021**, 80, 6509.
- [32] B. Su, H. Chen, P. Chen, G. Bian, K. Liu, W. Liu, *IEEE Trans. Ind. Inf.* **2020**, 17, 4084.
- [33] S. Deutsch, V. Christlein, S. Berger, C. Buerhop-Lutz, A. Maier, F. Gallwitz, C. Riess, *Sol. Energy* **2019**, 185, 455.
- [34] M. Mayr, M. Hoffmann, A. Maier, V. Christlein, in *2019 IEEE Inter. Conf. Image Processing (ICIP)*, IEEE, Piscataway, NJ **2019**, pp. 1885–1889.
- [35] H. Chen, S. Wang, J. Xing, in *2019 Chinese Automation Congress (CAC)*, IEEE, Piscataway, NJ **2019**, pp. 2565–2569.
- [36] Y. Zhao, K. Zhan, Z. Wang, W. Shen, *Prog. Photovoltaics: Res. Appl.* **2021**, 29, 471.
- [37] A. Ahmad, Y. Jin, C. Zhu, I. Javed, A. Maqsood, M. W. Akram, *IET Renewable Power Gener.* **2020**, 14, 2693.
- [38] A. Chindarkkar, S. Priyadarshi, N. S. Shiradkar, A. Kottantharayil, R. Velmurugan, in *2020 47th IEEE Photovoltaic Specialists Conf. (PVSC)*, IEEE, Piscataway, NJ **2020**, pp. 1612–1616.
- [39] E. Sovetkin, E. J. Achterberg, T. Weber, B. E. Pieters, *IEEE J. Photovoltaics* **2020**, 11, 444.
- [40] M. W. Akram, G. Li, Y. Jin, X. Chen, C. Zhu, X. Zhao, A. Khaliq, M. Faheem, A. Ahmad, *Energy* **2019**, 189, 116319.
- [41] M. R. U. Rahman, H. Chen, *IEEE Access* **2020**, 8, 40547.
- [42] X. Zhang, T. Hou, Y. Hao, H. Shangguan, A. Wang, S. Peng, *IEEE Access* **2021**, 9, 62093.
- [43] A. V. de Oliveira, M. Aghaei, R. Rüther, in *Proc. 36th European Photovoltaic Solar Energy Conf. and Exhibition*, Marseille, France **2019**, pp. 9–13.
- [44] L. Liu, Y. Zhu, M. R. U. Rahman, P. Zhao, H. Chen, in *2019 2nd China Symp. Cognitive Computing and Hybrid Intelligence (CCHI)*, IEEE, Piscataway, NJ **2019**, pp. 292–297.
- [45] P. Kunze, J. Greulich, S. Rein, K. Ramspeck, M. Hemsendorf, A. Vetter, M. Demant, presented at *37th European PV Solar Energy Conf. Exhibition*, Lisbon, Portugal **2020**, Vol. 7, p. 11.
- [46] G. Huang, Z. Liu, L. Van Der Maaten, K. Q. Weinberger, in *Proc. IEEE Conf. Computer Vision and Pattern Recognition*, IEEE, Piscataway, NJ **2017**, pp. 4700–4708.
- [47] *Advances in Neural Information Processing Systems*, Vol. 32 (Eds: A. Paszke, S. Gross, F. Massa, A. Lerer, J. Bradbury, G. Chanan,

T. Killeen, Z. Lin, N. Gimsheine, L. Antiga, A. Desmaison, A. Kopf, E. Yang, Z. DeVito, M. Raison, A. Tejani, S. Chilamkurthy, B. Steiner, L. Fang, J. Bai, S. Chintala, I. H. Wallach, H. Larochelle, A. Beygelzimer, F. d'Alché-Buc, E. Fox, R. Garnett), Curran Associates, Inc., Vancouver, Canada **2019**, pp. 8024–8035,

<http://papers.neurips.cc/paper/9015-pytorch-an-imperative-style-high-performance-deep-learning-library.pdf>.

[48] D. P. Kingma, J. Ba, arXiv preprint arXiv:1412.6980 **2014**.

[49] M. Demant, T. Welschehold, S. Kluska, S. Rein, *IEEE J. Photovoltaics* **2015**, 6, 136.